Research Square

Preprints are preliminary reports that have not undergone peer review.
They should not be considered conclusive, used to inform clinical practice,
or referenced by the media as validated information.

Enhancing the Therapeutic Ratio in Prostate LDR Brachytherapy: A TOPAS Monte Carlo Investigation ofNanoparticle Radiosensitization

Shahab Atefi

Shahab.atefi01@universitadipavia.it

University of Pavia

Payman Rafiepour

Persian Gulf University

Parvin Ahmadi

Shahed University

Research Article

Keywords: Dose Enhancement Factor, Nanoparticle Radiosensitization, Brachytherapy, Dose Volume Histogram, TOPAS

Posted Date: August 25th, 2026

DOI: https://doi.org/10.21203/rs.3.rs-10499744/v1

License: This work is licensed under a Creative Commons Attribution 4.0 International License.
Read Full License

Additional Declarations: No competing interests reported.

Enhancing the Therapeutic Ratio in Prostate LDR Brachytherapy: A TOPAS Monte Carlo Investigation of Nanoparticle Radiosensitization

Shahab Atefi[1*], Payman Rafiepour[2], Parvin Ahmadi[3]

1. Department of Physics, University of Pavia, Italy.
2. School of Engineering, Persian Gulf University, Mahini Ave, Bushehr 7516913817, Iran.
3. Department of Physics, Shahed University, Tehran, Iran.

*Corresponding author: Shahab Atefi, email: Shahab.atefi01@universitadipavia.it

Abstract

This Monte Carlo study evaluates and compares the radiosensitization potential of gold (Au) and platinum (Pt) nanoparticles (NPs) in prostate low-dose-rate (LDR) brachytherapy using ^{125}I and ^{103}Pd sources. Using the TOPAS Monte Carlo software, Au and Pt NPs (30 and 100 nm) were uniformly distributed within a tumor volume at concentrations of 7, 18, and 30 mg/g within a modified MIRD male phantom. Dose enhancement factors (DEFs) and dose volume histograms (DVHs) were calculated for both source types. Au NPs consistently outperformed Pt NPs, with maximum DEFs of 2.58 for Au versus 2.53 for Pt (^{125}I, 30 mg/g, 100 nm). DEF increased with concentration and NP size, with ^{125}I yielding greater enhancement than ^{103}Pd due to its lower photon energy. DVH analysis demonstrated selective tumor dose escalation (tumor Dmean increased from 239.8 Gy to 282.2 Gy for Pt with ^{103}Pd) with negligible impact on organs at risk. Photoelectric energy deposition increased by up to 20.7-fold with NP addition, correlating with observed DEF trends. In conclusions both Au and Pt NPs significantly enhance tumor dose in LDR brachytherapy while sparing adjacent organs, supporting an improved therapeutic ratio. The near-equivalence of Au and Pt NP performance suggests Pt may represent a viable, cost-effective alternative for clinical translation. These findings provide a dosimetric foundation for future experimental and clinical investigations.

Keywords: Dose Enhancement Factor; Nanoparticle Radiosensitization; Brachytherapy; Dose Volume Histogram; TOPAS

1. Introduction

One of the most common diagnosed malignancies among men worldwide is the prostate cancer (Kratzer et al., 2025). Among the curative treatment options for localized disease, low-dose-rate (LDR) brachytherapy is as a highly effective modality. This technique involves the permanent implantation of miniature radioactive seeds, typically employing low-energy iodine-125 (^{125}I) or palladium-103 (^{103}Pd) radioisotopes, to deliver a highly conformal radiation dose to the tumor while minimizing exposure to nearby organs at risk (OARs), such as bladder, urethra, and rectum (Skowronek, 2017). Owing to their reduced photon penetration range compared to higher-energy sources like iridium-192 and cobalt-60, these low-energy emitters are particularly advantageous for treating tumors situated in close proximity to radiosensitive structures.

In recent years, the integration of high-atomic-number nanoparticles (NPs) into radiation therapy has attracted considerable interest as a means to improve the therapeutic ratio. When irradiated by kilovoltage photon beams, high-atomic-number NPs such as gold (Au) amplify the local radiation dose primarily via an increased photoelectric effect, followed by the emission of Auger electrons and photoelectrons. The net consequence is a localized elevation in absorbed dose within NP-laden tumor regions, which is anticipated to improve tumor control probability without commensurately increasing the dose burden to surrounding healthy tissues (Lin et al., 2014; Laprise-Pelletier et al., 2018).

Given the stochastic nature of photon interactions and the complex, microscopic patterns of energy deposition they produce, Monte Carlo (MC) methods have become indispensable in modern radiation physics and dosimetry. Unlike deterministic analytical approaches, MC simulations accurately model particle transport and secondary electron production across heterogeneous media, enabling the investigation of interaction mechanisms that are challenging or infeasible to probe experimentally. Furthermore, MC simulations offer a robust computational platform for validating clinical treatment plans and exploring innovative radiosensitization strategies (Adhikari et al., 2025).

Numerous MC studies have quantified the dose enhancement factor (DEF) associated with Au NPs during LDR brachytherapy. Preclinical findings and simulation data indicate that Au NPs can potentiate radiation dose up to 300%, contingent upon the source energy, NP type, size, and concentration (Cho et al., 2009; 2010; Ghorbani et al., 2013; Ngwa et al., 2013; Lin et al., 2014; Asadi et al., 2015; 2016; Brivio et al., 2017; Rezaei et al., 2017; Moradi et al., 2021; Movahedizade and Sajjadi, 2025; Moeini et al., 2026).

While recent MC investigations have largely focused on microscopic (cellular) dose deposition (Taheri et al., 2023), the present macroscopic study offers a distinct advantage by enabling the direct computation of clinically relevant metrics, namely dose-volume histograms (DVHs), thereby facilitating a quantitative comparison between tumor and OAR doses. However, no prior investigation has systematically evaluated platinum (Pt) NPs as potential radiosensitizers for prostate LDR brachytherapy using ^{125}I and ^{103}Pd sources, while concurrently linking DEF to DVHs. Given its comparable atomic number (Pt: 78 vs. Au: 79) and density (Pt: 21.45 g/cm^3 vs. Au: 19.32 g/cm^3), Pt NPs may exhibit differential dose-enhancement properties that could be exploited for therapeutic gain.

To address this knowledge gap, the present simulation study incorporates both Au and Pt NPs, varying in size and concentration, in conjunction with ^{125}I and ^{103}Pd LDR brachytherapy

sources. The DEF and DVH metrics are calculated to quantify the dose enhancement within NP-containing tumor voxels, thereby providing a comparative assessment of the radiosensitization potential of these two heavy metals across different photon energies.

2. Methods

2.1. Simulation Platform

MC simulations were performed using TOPAS (Tool for Particle Simulation) (Perl et al., 2012; Faddegon et al., 2020), a powerful MC platform built upon the Geant4 toolkit (Agostinelli et al., 2003; Allison et al., 2016), specifically designed for applications in medical physics research. The present study employed OpenTOPAS version 4.0, obtained from the official GitHub repository of the TOPAS collaboration (https://github.com/OpenTOPAS), which represents a development lineage from TOPAS 3.9.

OpenTOPAS provides a user-friendly, parameterized interface that eliminates the need for C++ programming, enabling precise modeling of particle transport and interactions through arbitrarily complex geometries. The software offers comprehensive functionalities, including geometry construction, physics process selection, particle tracking, and event-by-event data extraction. It is well-validated for LDR brachytherapy simulations (Poher et al., 2023).

2.2. Physics List

Photon and electron interactions were modeled using the *g4em-livermore* TOPAS module, which is based on the G4EmLivermorePhysics class in Geant4 and implements the Livermore low-energy electromagnetic model (Cullen et al., 1997). This physics list is specifically optimized for photon and electron energies down to approximately 250 eV, making it particularly well-suited for LDR brachytherapy applications involving low-energy sources (^{125}I and ^{103}Pd). Photoelectric absorption, Compton scattering, pair production, and Rayleigh scattering processes were implemented for photons. Bremsstrahlung, ionization, multiple scattering, and excitation processes were implemented for electrons and positrons.

To account for radiobiological effects at the nanoscale, the *g4decay* module (based on the G4DecayPhysics class in Geant4) was incorporated into the physics list to enable atomic de-excitation processes. This module simulates fluorescence X-ray emission and Auger electron release following inner-shell ionization events.

To optimize the trade-off between computational efficiency and dosimetric accuracy, four distinct range cut-off thresholds were applied for secondary particles: 1 nm (for NP region), 1 μm (for Tumor region), 0.2 mm (for OARs), and 1 mm (for other organs and surrounding environment). When a particle's range falls below the defined cut-off threshold in a given region, its tracking is terminated, and the remaining kinetic energy is deposited locally at the point of termination.

2.3. LDR Brachytherapy Sources

Imagyn IS-12501 ^{125}I seed (Rivard et al., 2004) and Bebig IsoSeed ^{103}Pd seed (Daskalov and Williamson, 2001) models were defined in this study. The ^{125}I seed was defined as a cylindrical encapsulation with a length of 4.5 mm (including 0.4 mm titanium end caps) and a radius of 0.4 mm. Radioactive ^{125}I was assumed to be uniformly coated on the surface of five silver

microspheres, each with a radius of 0.3 mm. The ^{103}Pd seed was modeled as a cylindrical encapsulation with a length of 4.56 mm (including 0.4 mm titanium end caps) and a radius of 0.4 mm. In this design, radioactive ^{103}Pd was coated onto the surface of a cylindrical annulus (radius: 0.3 mm) composed of Al_2O_3 (density: 2.88 g/cm^3). Both seeds have a 0.05-mm thick titanium encapsulation, which effectively absorbs all emitted electrons, making them pure photon-emitting sources. The active lengths of the Imagyn IS-12501 and Bebig IsoSeed were 3.4 and 3.5 mm, respectively. Comprehensive geometrical specifications for the ^{125}I and ^{103}Pd seed models are detailed in Refs. (Rivard et al., 2004; Daskalov and Williamson, 2001). The recommended photon energy spectra for both sources, as used in this study, are presented in Table 2 (Rivard et al., 2004).

Table 2 Photon energy spectra for ^{125}I and ^{103}Pd brachytherapy sources, as recommended for dosimetric calculations (Rivard et al., 2004).

^{103}Pd		^{125}I	
Energy (MeV)	Branching ratio (%)	Energy (MeV)	Branching ratio (%)
0.020074	22.4	0.027202	40.6
0.020216	42.3	0.027472	75.7
0.022720	10.4	0.030980	20.2
0.023180	1.94	0.031710	4.39
0.039750	0.068	0.035492	6.68
0.294980	0.003		
0.357500	0.022		
0.497100	0.004		

Four LDR brachytherapy sources were located at the center of the tumor volume with center to center distance of 1 cm. While this arrangement LDR source does not reflect clinical practice, wherein multiple seeds are typically implanted in a structured array, this simplification was adopted for two primary reasons. First, prior studies have demonstrated that the precise spatial distribution of seeds within the tumor does not significantly influence the dose to OARs (Furtado et al., 2016; Orabi, 2026). Second, limiting the simulation to a simple arrangement permitted the use of a smaller tumor volume, thereby substantially reducing computational time and resource requirements. To prevent any spatial interference or overlapping geometry conflicts between the brachytherapy seeds and the NP volumes, all seeds were implemented using TOPAS's "*LayeredMassGeometryWorlds*" parameter, which allows independent geometries to coexist in identical spatial coordinates without overlapping (Enger et al., 2012).

Figure 2a presents schematic cross-sectional views of the simulated ^{125}I and ^{103}Pd seeds, while Figure 2b illustrates the seed positioning at the center of the tumor volume.

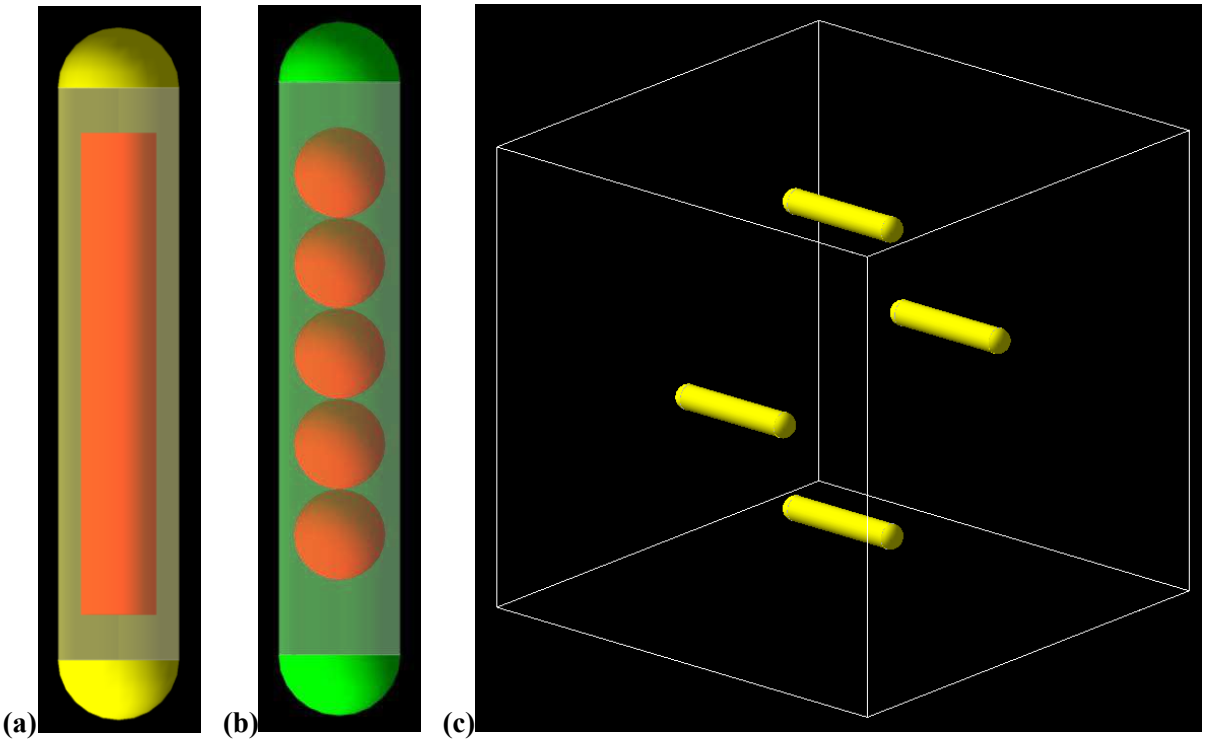


Fig. 2 Schematic representation of the simulated LDR brachytherapy sources and their placement within the tumor geometry. **(a)** Bebig IsoSeed ^{103}Pd seed; **(b)** Imagyn IS-12501 ^{125}I seed; **(c)** positioning of a single seed at the center of the tumor volume.

2.4. Source Validation

To validate the accuracy of our TOPAS simulation, dosimetric parameters were computed in accordance with the American Association of Physicists in Medicine (AAPM) TG-43U1 protocol (Rivard et al., 2004) and compared against the reference data for each seed. The air kerma strength *(S_k)* is obtained by calculating the air kerma rate $\dot{K}_\delta(d)$ at radial distances along the transverse axis of the seed in air, scaled by the square of the distance:

$$S_k = \dot{K}_\delta(d)\, d^2 \quad (1)$$

The dose rate constant, (Λ), is the ratio of the dose rate at a designated reference point (r_0 = 1 cm, θ_0 = 90 degrees) on the transverse axis to the S_k obtained above:

$$\Lambda = \frac{\dot{D}(r_o.\theta_o)}{S_k} \quad (2)$$

Λ is dependent on both the radioisotope and the specific seed design, and has the unit of cm^{-2}. The geometric function, $G(r,\theta)$, considers the spatial distribution of radioactive material in the seed. According to the line source approximation:

$$G(r.\theta) = \frac{\beta}{L\, r sin\theta} \quad . \quad if \quad \theta \neq 0^o \quad (3)$$

$$G(r.\theta) = (r^2 - \frac{L^2}{4})^{-1} \, . \quad if\ \theta = 0^o \quad (4)$$

Where L represents the effective active length of the seed and β is the angle subtended by the L at the point of interest (r,θ).

The radial dose function, $g(r)$, describes the radiation attenuation along the transverse axis (θ_0 = 90 degrees) as it propagates through tissue, excluding the effects of geometric falloff. It is calculated over a radial distance of 0.5 cm to 10 cm from the source center (Rivard et al., 2004):

$$g(r) = \frac{\dot{D}(r.\theta_0)\, G(r_0 .\theta_0)}{\dot{D}(r_0.\theta_0)\, G(r.\theta)} \quad (5)$$

2.5. Phantom Geometry

The trunk section of the male MIRD (Medical Internal Radiation Dose) phantom Cristy and Eckerman, 1987) was constructed within the TOPAS simulation environment. It remains widely utilized in computational dosimetry due to its simplicity and efficiency relative to voxelized phantoms, making it particularly suitable for comparative evaluations. The original MIRD phantom does not include several organs critical to prostate brachytherapy dosimetry. Accordingly, we extended the phantom by incorporating the prostate, urethra, and rectum as additional anatomical structures (Figure 2). Bladder was modeled as a spherical volume of water with a diameter of 6 cm. Rectum was defined as a hollow, conical tube with a length of 10 cm, a radius of 1.25 cm, and a wall thickness of 3 mm. The lumen was filled with air. Prostate was modeled as a spherical volume with a diameter of 5.4 cm, containing both the urethra and the tumor. Urethra was modeled as a cylindrical volume with a radius of 0.75 mm and a length of 5.4 cm, traversing the prostate along its central axis. Finally, the tumor was defined as a cubic volume with an edge length of 1.5 cm embedded within the prostate. The tumor was assigned soft tissue composition with a density of 1.0 g/cm^3. The elemental composition by mass fraction was adopted from ICRU Report 44 (Snyder et al., 1975) and consisted of: oxygen (63.02%), carbon (23.22%), hydrogen (10.45%), nitrogen (2.488%), sulfur (0.199%), potassium (0.199%), chlorine (0.134%), phosphorus (0.133%), sodium (0.113%), calcium (0.023%), magnesium (0.013%), iron (0.005%), and zinc (0.003%).

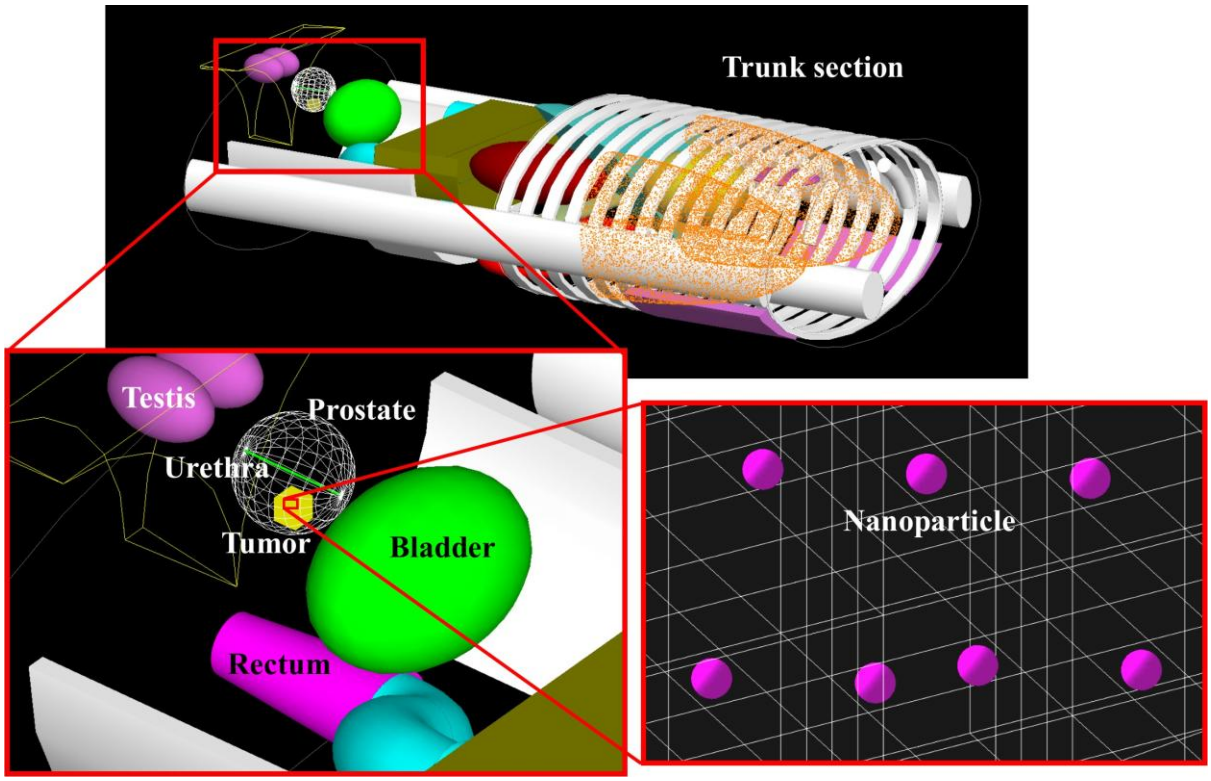


Figure 2. The modified trunk section of the MIRD male phantom illustrating the anatomical relationship between the prostate, tumor (1.5×1.5×1.5 cm^3 cube within the prostate), rectum, bladder, and urethra.

2.6. NP Distribution

Au and Pt NPs were uniformly distributed in the tumor at 7, 18, and 30 mg/g concentrations in a regular lattice arrangement. Each NP is placed inside a small cubic voxel. Then, billions of voxels were repeated in three-dimensions filling-up the cubic tumor. While this regular lattice structure, which provides uniform inter-NP spacing, considers the size of NPs, it does not explicitly simulate Auger electron track structures within individual NPs. However, this macroscopic implementation offers clinically relevant estimates of mean DEFs, which is useful for treatment planning considerations.

Table 3 lists the total number of NPs in the tumor ($1.5 \times 1.5 \times 1.5$ cm^3) for various NP material, size, and concentrations. The voxel size, defined as the side length of the cubic microscopic voxel containing a single NP in the regular lattice is also provided.

Table 3. The total number of Au and Pt nanoparticles in the tumor ($1.5 \times 1.5 \times 1.5$ cm^3) with 7, 18, and 30 mg/g concentrations and 30 and 100 nm sizes.

Material	Size (nm)	Concentration (mg/g)	Voxel size (μm)	Number
Au	30	7	0.305142	1.18787e+14
		18	0.222729	3.05451e+14
		30	0.187857	5.09085e+14
	100	7	1.017140	3.20725e+12
		18	0.742430	8.24722e+12
		30	0.626190	1.37454e+13
Pt	30	7	0.315967	1.06991e+14
		18	0.230631	2.75120e+14
		30	0.194522	4.58533e+14
	100	7	1.053220	2.88877e+12
		18	0.768768	7.42826e+12
		30	0.648404	1.23804e+13

2.7. DEF Calculation

Let D_{NP} and D_0 represent the tumor dose with and without the presence of NPs, respectively. Then, DEF was quantified using Equation 6:

$$DEF = {}^{D_{NP}}/_{D_0} \tag{6}$$

A DEF greater than unity indicates dose escalation, while a DEF equal to unity corresponds to no net enhancement. For each simulation condition, two independent simulation runs were performed. Each run was initialized with a distinct, non-repeating random seed to ensure statistical independence. The mean DEF were subsequently calculated across the runs for all reported values. A total of 2×10^8 primary photons were simulated per run for each source condition. This number of histories ensures that the statistical uncertainty remained below 0.05% and 1% within the tumor and OARs, respectively.

3. Result

The dose rate constants (Λ) calculated for the Imagyn IS-12501 ^{125}I seed and Bebig IsoSeed ^{103}Pd seed are presented in Table 4. The radial dose functions, g(r), are shown in Figure 3, with the maximum deviation of 2.9% observed at radial distances of 4 and 10 cm for the ^{103}Pd seed. As demonstrated, the TOPAS values exhibit good agreement with the reference data, with relative differences consistently below 3% (Rivard et al., 2004; Daskalov and Williamson, 2001).

Table 4**.** Dose rate constant for the Imagyn IS-12501 ^{125}I and Bebig IsoSeed ^{103}Pd seeds.

Source	This study (cm^{-2})	Reference data (cm^{-2})	Relative difference (%)
Imagyn IS-12501 ^{125}I	0.963 ± 0.01	0.940 (Rivard et al., 2004)	2.44
Bebig IsoSeed ^{103}Pd	0.675 ± 0.01	0.664 (Daskalov and Williamson, 2001)	1.65

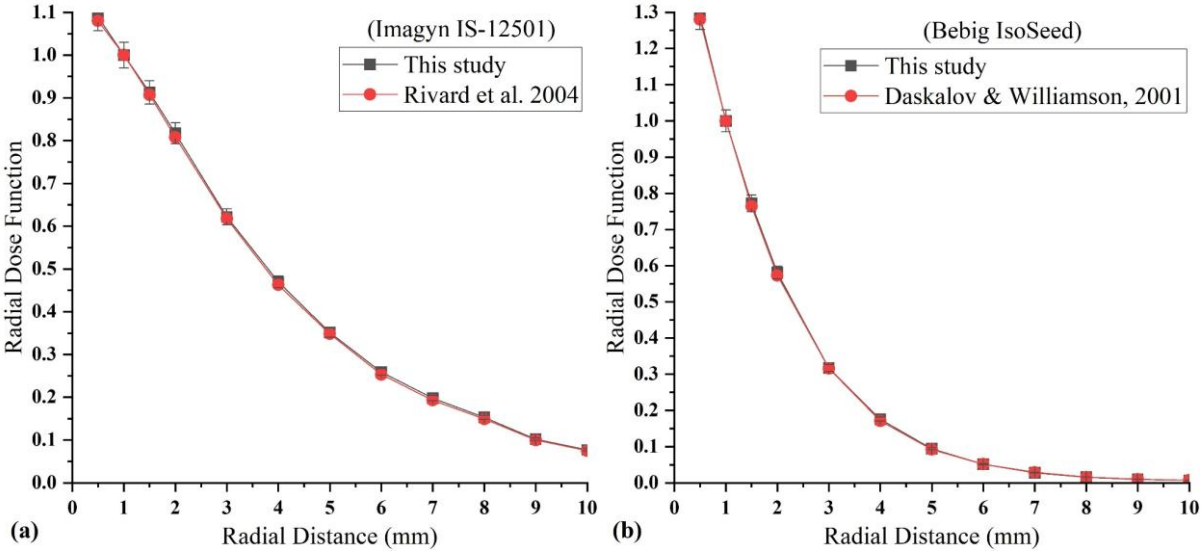


Figure 3. Radial dose function, g(r), comparing the TOPAS Monte Carlo results with reference data (Rivard et al., 2004; Daskalov and Williamson, 2001) for the **(a)** Imagyn IS-12501 ^{125}I and **(b)** Bebig IsoSeed ^{103}Pd seeds.

The DEFs associated with Au and Pt NPs at 7, 18, and 30 mg/g concentrations and NP sizes of 30 and 100 nm are presented in Figure 4 for both ^{125}I and ^{103}Pd sources.

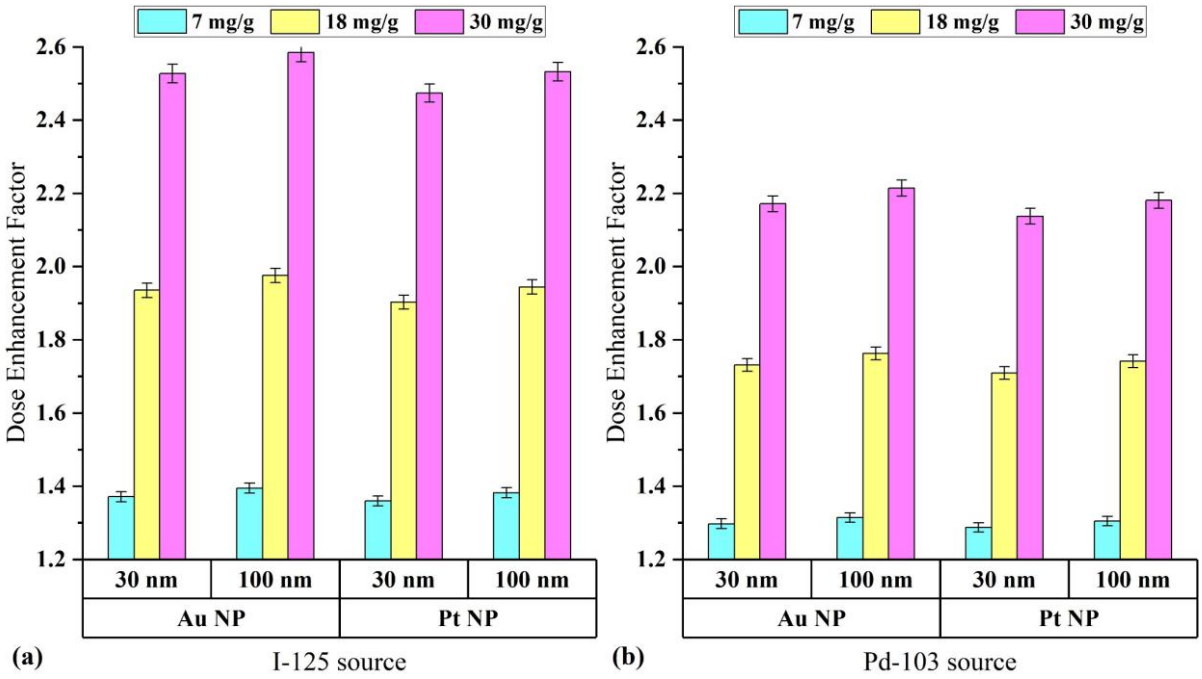


Figure 4. Dose enhancement factors for Au and Pt nanoparticles (NPs) at 7, 18, and 30 mg/g concentrations and NP sizes of 30 and 100 nm for the **(a)** ^{125}I and **(b)** ^{103}Pd sources.

Figure 5 compares the DVHs of the tumor and OARs for the baseline case in which no NPs are present. Panel (a) shows the DVHs for the ^{125}I source, while Panel (b) shows the corresponding data for the ^{103}Pd source. Similar DVHs for the cases with Au and Pt NPs are presented in Figures 6 and 7, respectively. To illustrate the maximum possible effect on DVHs, only the 100 nm NPs at 30 mg/g concentration were considered for these comparisons.

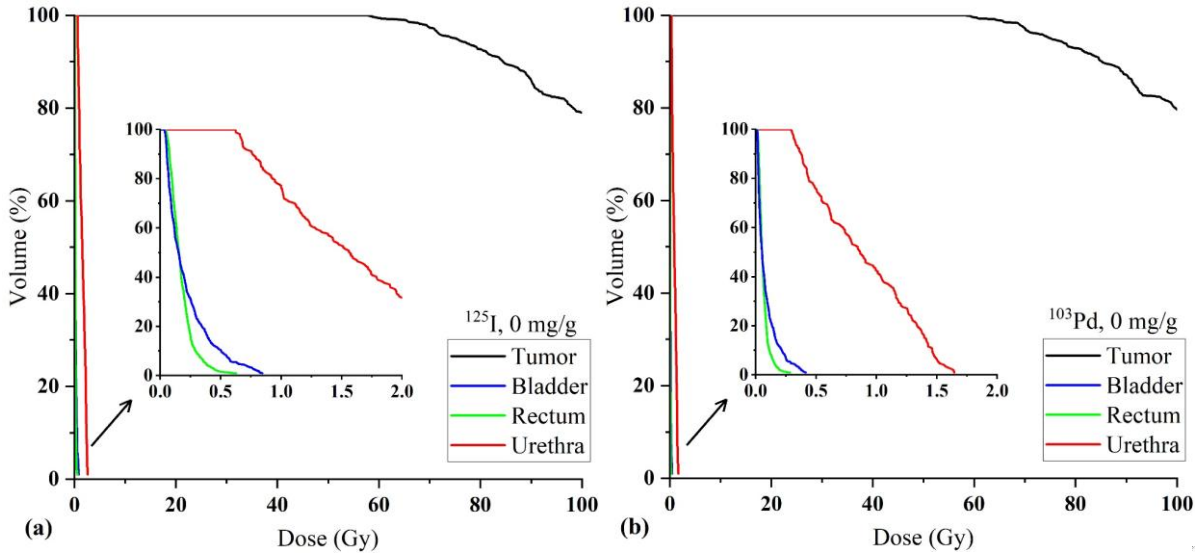


Figure 5. Dose volume histograms (DVHs) of the tumor, bladder, rectum, and urethra for the **(a)** ^{125}I and **(b)** ^{103}Pd seeds in the absence of nanoparticles.

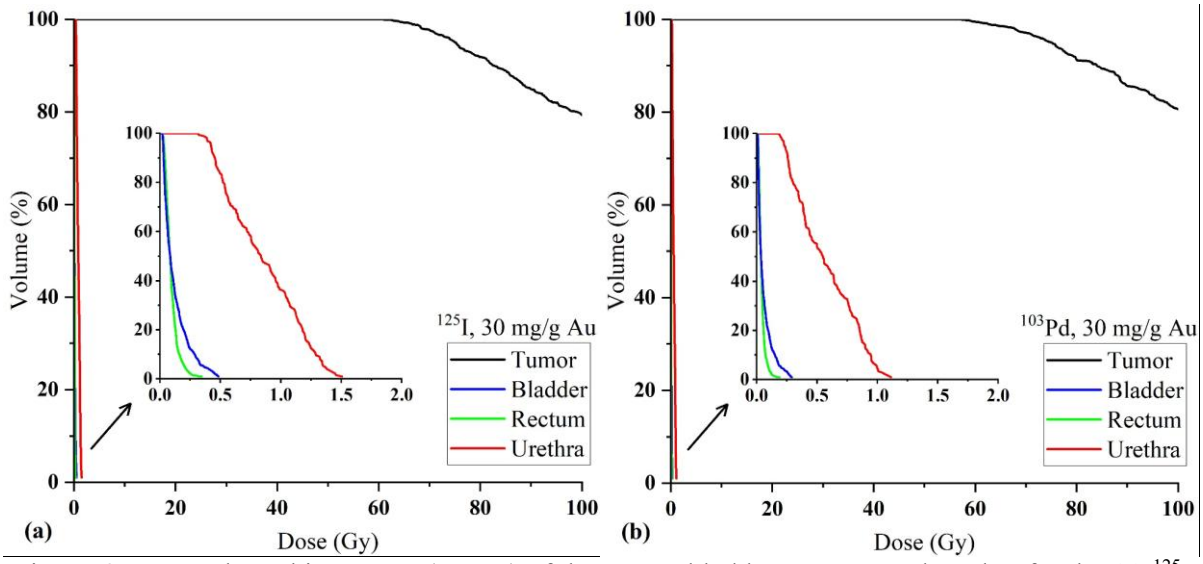


Figure 6. Dose volume histograms (DVHs) of the tumor, bladder, rectum, and urethra for the **(a)** ^{125}I and **(b)** ^{103}Pd seeds in the presence of 30 mg/g gold (Au) nanoparticles (100 nm size).

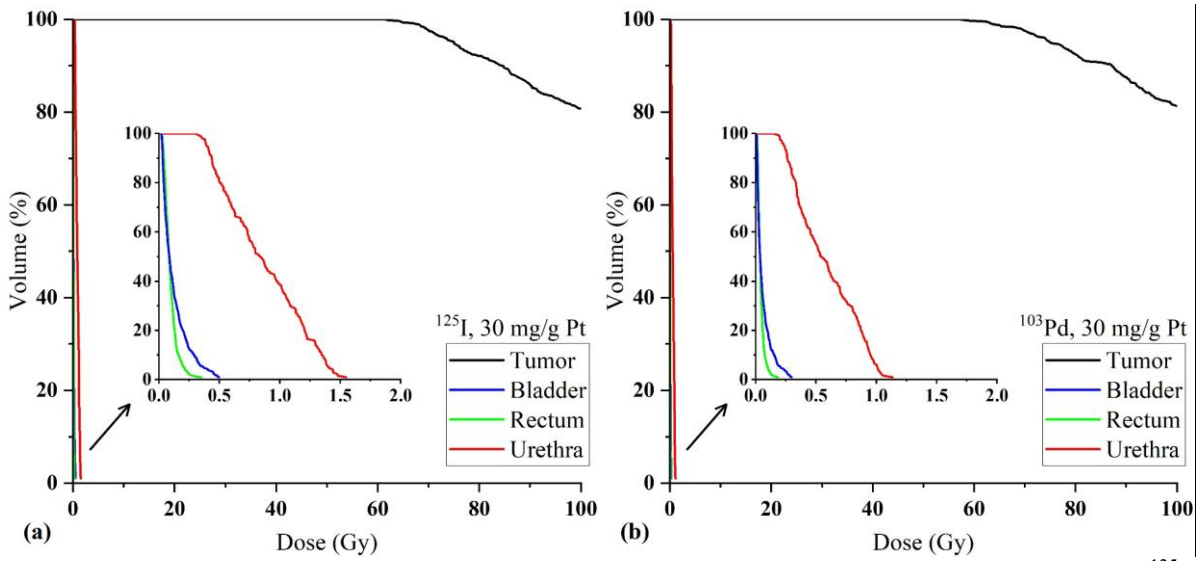


Figure 7. Dose volume histograms (DVHs) of the tumor, bladder, rectum, and urethra for the **(a)** ^{125}I and **(b)** ^{103}Pd seeds in the presence of 30 mg/g platinum (Pt) nanoparticles (100 nm size).

Quantitative DVH metrics, including the minimum dose (Dmin), maximum dose (Dmax), and mean dose (Dmean), were extracted from the DVHs and are summarized in Table 5 for both ^{125}I and ^{103}Pd LDR sources. As with the DVH comparisons, only the 30 mg/g NPs with a size of 100 nm were considered to demonstrate the maximum possible impact on these dosimetric endpoints.

Table 5. DVH metrics such as Dmax, Dmin, and Dmean for Au and Pt nanoparticle (NP) (30 mg/g NPs with a size of 100 nm) for ^{125}I and ^{103}Pd LDR sources.

NP	DVH metric	^{125}I				^{103}Pd			
		Tumor	Bladder	Rectum	Urethra	Tumor	Bladder	Rectum	Urethra
None	Dmax	1656	0.84	0.63	2.64	1756	0.41	0.28	1.64

	Dmin	57.86	0.03	0.04	0.62	58.16	0.01	0.01	0.29
	Dmean	239.8	0.21	0.17	1.56	251.3	0.08	0.06	0.89
Au	Dmax	2113	0.48	0.34	1.51	2141	0.29	0.19	1.11
	Dmin	60.45	0.02	0.02	0.31	57.10	0.01	0.01	0.18
	Dmean	248.5	0.12	0.09	0.85	282.8	0.06	0.04	0.57
Pt	Dmax	2087	0.49	0.35	1.55	2143	0.30	0.18	1.13
	Dmin	61.62	0.02	0.02	0.30	57.25	0.01	0.01	0.14
	Dmean	282.2	0.12	0.09	0.86	284.1	0.06	0.04	0.58

Table 6 presents the normalized energy deposition (eV per event) resulting from photoelectric interactions within the tumor, with and without 30 mg/g Au and Pt NPs (100 nm size) for both ^{125}I and ^{103}Pd LDR sources

Table 6. Normalized energy deposition (eV per event) due to photoelectric interactions within the tumor for various nanoparticle materials, sizes, and concentrations, for ^{125}I and ^{103}Pd LDR sources.

Material	size (nm)	Concentration (mg/g)	^{125}I	^{103}Pd
None	-	-	25.156	56.557
Au	30	7	141.56	274.37
		18	318.11	593.51
		30	503.29	914.63
	100	7	148.76	287.09
		18	330.78	615.57
		30	521.31	945.30
Pt	30	7	134.81	141.78
		18	300.98	313.91
		30	475.59	493.30
	100	7	262.64	274.65
		18	563.86	586.35
		30	868.88	899.88

4. Discussion

According to Figure 4, the results demonstrate aa more or less linear relationship between NP concentration and DEF for both Au and Pt NPs, across both source types and NP sizes. For ^{125}I seeds with 30 nm Au NPs, DEF increased from 1.37 at 7 mg/g to 2.53 at 30 mg/g, representing an 84.6% increase. Similarly, for ^{103}Pd with 30 nm Au NPs, DEF rose from 1.30 to 2.17 (66.9% increase). This concentration-dependent enhancement is consistent with previous MC results (Cho et al., 2009; 2010; Ghorbani et al., 2013; Ngwa et al., 2013; Asadi et al., 2015; 2016; Brivio et al., 2017; Rezaei et al., 2017; Moradi et al., 2021; Movahedizade and Sajjadi, 2025; Moeini et al., 2026) and is attributed to the increased number of high-atomic-number atoms available for photoelectric interactions, leading to greater secondary electron production and localized energy deposition. The near-linear relationship suggests that within the clinically relevant concentration range of 7-30 mg/g, dose enhancement scales predictably with NP loading, facilitating potential treatment planning optimization.

The results also reveal that larger NPs consistently produced slightly higher DEFs than smaller NPs (100 nm vs. 30 nm) at equivalent concentrations. For ^{125}I with Au NPs at 30 mg/g, DEF improved from 2.53 (30 nm) to 2.58 (100 nm), a marginal but consistent enhancement of approximately 2.0%. This size-dependent effect was observed across both materials and source types, albeit with modest magnitude. Several factors may explain the observed trend. First, larger NPs possess a greater total cross-sectional area for photon interactions, potentially compensating for the reduced surface area. Second, the physical range of emitted Auger electrons and photoelectrons, on the order of nanometers to micrometers, may be better matched to the dimensions of 100 nm NPs, allowing for more efficient local energy deposition before electron escape. Third, the macroscopic homogenization approach, which assumes uniform NP distribution, may not fully capture the nanoscale spatial effects that would favor smaller particles in heterogeneous cellular environments (Movahedizade and Sajjadi, 2025). The relatively modest size effect observed in our study suggests that for macroscopic dose enhancement, NP concentration is a more significant determinant than size, a finding with practical implications for clinical translation.

Au NPs consistently outperformed Pt NPs in terms of DEF across all conditions. For ^{125}I at 30 mg/g and 100 nm size, DEF for Au was 2.58 compared to 2.53 for Pt, a relative difference of approximately 2.0%. For ^{103}Pd at the same conditions, the difference was 2.21 for Au versus 2.18 for Pt (approximately 1.4%). While statistically modest, this consistent trend is physically plausible given the slightly higher atomic number of Au (Z = 79) compared to Pt (Z = 78) and its marginally greater density (19.32 vs. 21.45 g/cm^3), which collectively enhance the photoelectric cross-section. However, the small magnitude of the difference suggests that the photoelectric cross-sections of these two adjacent high-atomic-number elements are sufficiently similar that other factors, such as NP geometry, surface chemistry, and cellular uptake, may play a more decisive role in clinical efficacy than atomic number alone.

The near-equivalence of Au and Pt NP performance in this macroscopic model opens interesting avenues for clinical consideration. Pt NPs, while yielding marginally lower DEFs, may offer advantages in terms of cost, biocompatibility, or tumor-targeting capabilities that could offset the slight dosimetric disadvantage. Future experimental studies comparing the biological efficacy of Au and Pt NPs in relevant preclinical models would be valuable to determine whether the small DEF difference translates into meaningful radiobiological outcomes.

A consistent finding across all conditions was the substantially greater DEF achieved with the ^{125}I source compared to ^{103}Pd. For 100 nm Au NPs at 30 mg/g, DEF was 2.58 for ^{125}I versus 2.21 for ^{103}Pd, representing a 16.7% relative enhancement. This energy-dependent effect is readily explained by the photon energy spectra of the two sources. ^{125}I emits lower-energy photons (predominantly ~27-35 keV) compared to ^{103}Pd (primarily ~20-23 keV with higher-energy emissions up to ~497 keV) (Table 2). The photoelectric cross-section scales approximately as Z^3/E^3, where E is the photon kinetic energy and Z is the atomic number. Consequently, the lower-energy photons from ^{125}I interact more efficiently with high-atomic-number NPs, generating a greater flux of photoelectrons and Auger electrons that contribute to localized dose enhancement.

The DEFs of this study are in accordance with previously published values, although direct quantitative comparisons are complicated by variations in simulation approaches, NP

definitions, source geometries, and tumor models. Table 7 summaries some of DEF values previously published for LDR brachytherapy.

Table 7. Comparison of representative DEF values reported in previous Monte Carlo studies for Au and Pt nanoparticles (NP) in brachytherapy.

Study	NP	Size (nm)	Conc. (mg/g)	Source	Application	DEF
Cho et al. (2009)	Au	-	7	^{125}I	Prostate	≤ 2.0
Asadi et al. (2015)	Au	-	7	^{125}I	Eye	≤ 2.1
Asadi et al. (2016)	Au	-	7	^{125}I / ^{103}Pd	Eye	1.94 / 1.62
Cho et al. (2010)	Au	-	7	^{125}I / ^{103}Pd	Various	1.87 / 1.58
Brivio et al. (2017)	Au	-	10-30	^{125}I	Prostate	≤ 2.0
Moradi et al. (2021)	Au	50	5-20	kV x-rays	Prostate	1.5–3.0
Ghorbani et al. (2013)	Au / Pt	-	7	^{125}I	Prostate	1.43 / 1.32
Movahedi & Sajjadi (2025)	Au	-	7	^{125}I / ^{103}Pd	Lung	~2.41 / ~1.91
Moieni et al. (2026)	Au	-	5-30	^{125}I / ^{103}Pd	Eye	3.29 / 2.20
Present Study	Au	30	7	^{125}I	Prostate	1.37
		100	30	^{125}I	Prostate	2.58
	Pt	100	30	^{125}I	Prostate	2.53

As shown in Table 7, the wide range of DEF values reported across these studies, from approximately 1.3 to 3.3, reflects the substantial dependence of dose enhancement on simulation methodology, NP characteristics (size, concentration, and distribution), source geometry, and the specific anatomical context of the tumor model. Despite this variability, several consistent trends emerge. First, the higher DEF obtained with ^{125}I compared to ^{103}Pd for a given NP type, as observed by Refs. (Cho et al., 2010; Asadi et al., 2016; Movahedi & Sajjadi, 2025; Moieni et al. 2026), is consistent with the results of the present study and is attributable to the lower photon energy of ^{125}I and consequently greater photoelectric interaction probability. Second, Ghorbani et al. (2013) calculated DEFs of up to 1.43 and 1.32 for 7 mg/g Au and Pt NPs, respectively, in prostate ^{125}I brachytherapy, values that are slightly lower than our corresponding DEFs of 1.37 (Au) and 1.36 (Pt) at the same concentration and 30 nm size. This minor discrepancy may arise from differences in simulation geometry, phantom configuration, or NP spatial distribution assumptions. The consistent observation across multiple independent studies that ^{125}I yields greater DEFs than ^{103}Pd reinforces the physical basis of NP-mediated radiosensitization and supports the clinical preference for ^{125}I in NP-enhanced LDR brachytherapy applications.

^{125}I has historically been the most widely used isotope for prostate LDR brachytherapy, and our results reinforce its suitability for NP-enhanced approaches. However, ^{103}Pd offers advantages in terms of higher dose rate and shorter half-life (17 days vs. 60 days for ^{125}I), which may be preferable for certain tumor histologies and treatment schedules. The moderate DEF achievable with ^{103}Pd (up to 2.21) suggests that NP-enhanced brachytherapy remains a viable option even with this isotope, albeit with somewhat reduced magnitude of dose escalation.

According to Figures 5-7 and Table 5, in the absence of NPs, the tumor received a mean dose of 239.8 Gy for ^{125}I and 251.3 Gy for ^{103}Pd, while OAR doses remained low (e.g., bladder Dmean: 0.21 Gy for ^{125}I, 0.08 Gy for ^{103}Pd). This favorable baseline dosimetric profile underscores the inherent conformality of LDR brachytherapy.

With the addition of 30 mg/g, 100 nm Au NPs, tumor Dmean increased substantially to 248.5 Gy (^{125}I) and 282.8 Gy (^{103}Pd), representing dose escalations of 3.6% and 12.5%, respectively. Pt NPs produced comparable tumor Dmean values of 282.2 Gy (^{125}I) and 284.1 Gy (^{103}Pd). Critically, OAR doses remained essentially unchanged with NP addition (e.g., bladder Dmean with Au NPs: 0.12 Gy for both sources). This differential effect, selective tumor dose escalation without commensurate OAR dose increase, is the hallmark of an improved therapeutic ratio and forms the radiobiological rationale for NP-mediated radiosensitization.

The greater relative increase in tumor Dmean for ^{103}Pd (12.5%) compared to ^{125}I (3.6%) with Au NPs is noteworthy, despite the lower absolute DEF values for ^{103}Pd. This apparent paradox may be explained by the baseline dose distributions: ^{103}Pd deposits dose more heterogeneously within the tumor, leaving greater "room" for NP-mediated dose escalation in underdosed regions. This observation highlights the importance of evaluating not only mean DEF but also the spatial distribution of dose enhancement, which is captured by DVH analysis.

The Dmax values in our study (e.g., 2113 Gy for ^{125}I with Au NPs) represent extremely high local doses within small voxels. While these values are unlikely to be clinically achievable or necessary, they reflect the intense, highly localized energy deposition in the immediate vicinity of NPs, the microscopic "hot spots" responsible for biological effect. The clinical relevance of these extreme Dmax values is debatable, and they should be interpreted with caution, as they may overestimate the biological impact in the absence of detailed cellular response modeling (Butler et al., 2016).

According to Table 6, for the no-NP baseline, ^{103}Pd exhibited higher photoelectric energy deposition (56.6 eV per event) than ^{125}I (25.2 eV per event), reflecting the greater probability of photoelectric interactions in soft tissue at lower photon energies. However, this baseline advantage for ^{103}Pd was reversed upon NP addition. At 30 mg/g, 100 nm Au NPs, photoelectric energy deposition increased dramatically to 945.3 eV per event for ^{103}Pd and 521.3 eV per event for ^{125}I, representing fold-increases of 16.7x and 20.7x, respectively. The higher fold-increase for ^{125}I explains its superior DEF performance, as the NP-mediated amplification of photoelectric interactions is proportionally greater relative to baseline.

Comparing Au and Pt NPs, the photoelectric energy deposition was consistently higher for Au across all conditions. At 30 mg/g, 100 nm NPs with ^{125}I, Au deposited 521.3 eV per event versus 868.9 eV for Pt with ^{103}Pd. The higher values for ^{103}Pd reflect its greater baseline photoelectric cross-section; however, the fold-enhancement relative to baseline was consistently superior for Au with ^{125}I. This interplay between baseline tissue interactions and NP-mediated amplification underscores the complexity of predicting DEF based solely on NP properties, highlighting the value of comprehensive MC simulations for optimizing clinical protocols.

5. Conclusion

In conclusion, this TOPAS MC study provides a comparative assessment of Au and Pt NP-mediated radiosensitization in prostate LDR brachytherapy. Both NP types significantly enhance tumor dose, with Au NPs consistently outperforming Pt NPs by a modest margin. DEF increases with NP concentration and, to a lesser extent, NP size, with the ^{125}I source yielding greater enhancement than ^{103}Pd due to its narrower photon energy range. DVH analysis reveals selective tumor dose escalation with negligible impact on OARs, supporting an improved

therapeutic ratio. While Pt NPs offer slightly lower DEFs than Au NPs, their near-equivalence suggests they may represent a viable alternative for NP-enhanced brachytherapy. These findings provide a dosimetric foundation for future experimental and clinical investigations of NP-mediated radiosensitization in prostate cancer.

Statements and Declarations

Funding
None.

Acknowledgments
None.

Competing Interests
The authors have no relevant financial or non-financial interests to disclose.

Ethics approval
Not applicable.

Consent to participate
Not applicable.

Consent to publish
Not applicable.

Availability of data
All data produced from this study will be available from the corresponding author on reasonable request.

Reference:

Adhikari, T., Montenegro, T., Jung, J. W., Oare, C., Fonseca, G., Beaulieu, L., ... & Ferreira, C. (2025). The use of Monte Carlo simulation techniques in brachytherapy: a comprehensive literature review. *Brachytherapy*, *24*(4), 564-621. https://doi.org/10.1016/j.brachy.2025.02.006

Agostinelli, S., Allison, J., Amako, K., Apostolakis, J., Araujo, H., Arce, P. et al. (2003). Geant4—a simulation toolkit. *Nucl. Instruments Methods Phys. Res. Sect. A Accel. Spectrometers, Detect. Assoc. Equip.* 506, 250–303. https://doi.org/10.1016/S0168-9002(03)01368-8

Allison, J., Amako, K., Apostolakis, J., Arce, P., Asai, M., Aso, T., ... & Yoshida, H. (2016). Recent developments in Geant4. *Nuclear instruments and methods in physics research section A: Accelerators, Spectrometers, Detectors and Associated Equipment*, *835*, 186-225. https://doi.org/10.1016/j.nima.2016.06.125

Asadi, S., Vaez-zadeh, M., Masoudi, S. F., Rahmani, F., Knaup, C., & Meigooni, A. S. (2015). Gold nanoparticle-based brachytherapy enhancement in choroidal melanoma using a full Monte Carlo model of the human eye. *Journal of applied clinical medical physics*, *16*(5), 344–357. https://doi.org/10.1120/jacmp.v16i5.5568

Asadi, S., Vaez-Zadeh, M., Vahidian, M., Marghchouei, M., & Masoudi, S. F. (2016). Ocular brachytherapy dosimetry for 103Pd and 125I in the presence of gold nanoparticles: a Monte Carlo study. *Journal of applied clinical medical physics*, *17*(3), 90–99. https://doi.org/10.1120/jacmp.v17i3.5945

Brivio, D., Nguyen, P. L., Sajo, E., Ngwa, W., & Zygmanski, P. (2017). A Monte Carlo study of I-125 prostate brachytherapy with gold nanoparticles: dose enhancement with simultaneous rectal dose sparing via radiation shielding. *Physics in medicine and biology*, *62*(5), 1935–1948. https://doi.org/10.1088/1361-6560/aa5bc7

Butler, W. M., & Merrick, G. S. (2016). Focal prostate brachytherapy with 103Pd seeds. *Physica Medica*, *32*(3), 459-464. https://doi.org/10.1016/j.ejmp.2016.03.012

Cho, S. H., Jones, B. L., & Krishnan, S. (2009). The dosimetric feasibility of gold nanoparticle-aided radiation therapy (GNRT) via brachytherapy using low-energy gamma-/x-ray sources. *Physics in medicine and biology*, *54*(16), 4889–4905. https://doi.org/10.1088/0031-9155/54/16/004

Cho, S., Jeong, J. H., Kim, C. H., & Yoon, M. (2010). Monte Carlo simulation study on dose enhancement by gold nanoparticles in brachytherapy. *J Korean Phys Soc*, *56*(6), 1754-1758. https://doi.org/10.3938/jkps.56.1754

Cristy, M., & Eckerman, K. F. (1987). *Specific Absorbed fractions of energy at various ages from internal photon sources: 1, Methods* (No. ORNL/TM-8381/V1). Oak Ridge National Lab. (ORNL), Oak Ridge, TN (United States).

Cullen DE, Hubbell JH, Kissel L (1997) EPDL97: the evaluated photo data library 97 version. Lawrence Livermore National Lab., CA (United States).

Daskalov, G. M., & Williamson, J. F. (2001). Monte Carlo-aided dosimetry of the new Bebig IsoSeed 103Pd interstitial brachytherapy seed. *Medical physics*, *28*(10), 2154–2161. https://doi.org/10.1118/1.1395035

Enger, S. A., Landry, G., D'Amours, M., Verhaegen, F., Beaulieu, L., Asai, M., & Perl, J. (2012). Layered mass geometry: a novel technique to overlay seeds and applicators onto patient geometry in Geant4 brachytherapy simulations. *Physics in medicine and biology*, *57*(19), 6269–6277. https://doi.org/10.1088/0031-9155/57/19/6269

Faddegon, B., Ramos-Méndez, J., Schuemann, J., McNamara, A., Shin, J., Perl, J., & Paganetti, H. (2020). The TOPAS tool for particle simulation, a Monte Carlo simulation tool for physics, biology and clinical research. *Physica medica*, *72*, 114–121. https://doi.org/10.1016/j.ejmp.2020.03.019

Furtado, M., Teles, P., Laporte, C., Khalfallah, N., Broggio, D., Costa, D., & Vaz, P. (2016). Dosimetric study of prostate brachytherapy, using Monte Carlo simulations and voxel phantoms. *Physica Medica*, *32*, 322. https://doi.org/10.1016/j.ejmp.2016.07.211

Ghorbani, M., Bakhshabadi, M., Golshan, A., & Knaup, C. (2013). Dose enhancement by various nanoparticles in prostate brachytherapy. *Australasian physical & engineering sciences in medicine*, *36*(4), 431–440. https://doi.org/10.1007/s13246-013-0231-z

Kratzer, T. B., Mazzitelli, N., Star, J., Dahut, W. L., Jemal, A., & Siegel, R. L. (2025). Prostate cancer statistics, 2025. *CA: a cancer journal for clinicians*, *75*(6), 485–497. https://doi.org/10.3322/caac.70028

Laprise-Pelletier, M., Simão, T., & Fortin, M. A. (2018). Gold Nanoparticles in Radiotherapy and Recent Progress in Nanobrachytherapy. *Advanced healthcare materials*, *7*(16), e1701460. https://doi.org/10.1002/adhm.201701460

Lin, Y., McMahon, S. J., Scarpelli, M., Paganetti, H., & Schuemann, J. (2014). Comparing gold nano-particle enhanced radiotherapy with protons, megavoltage photons and kilovoltage photons: a Monte Carlo simulation. *Physics in medicine and biology*, *59*(24), 7675–7689. https://doi.org/10.1088/0031-9155/59/24/7675

Movahedizade, E., & Sajjadi, Z. (2025). A multi-scale Monte Carlo simulation on nanoparticle dose enhancement for a lung tumour treated with low-energy brachytherapy. *Radiation and Environmental Biophysics*, *64*(4), 681-696. https://doi.org/10.1007/s00411-025-01152-0

Moeini, S. M., Sina, S., Rafiepour, P., & Siavashpour, Z. (2026). Monte Carlo simulation of uveal melanoma treatment by ocular plaque brachytherapy using gold nanoparticles. *Radiation and environmental biophysics*, *65*(1), 501–518. https://doi.org/10.1007/s00411-026-01206-x

Moradi, F., Sani, S. A., Khandaker, M. U., Sulieman, A., & Bradley, D. A. (2021). Dosimetric evaluation of gold nanoparticle aided intraoperative radiotherapy with the Intrabeam system using Monte Carlo simulations. *Radiation Physics and Chemistry*, *178*, 108864. https://doi.org/10.1016/j.radphyschem.2020.108864

Ngwa, W., Korideck, H., Kassis, A. I., Kumar, R., Sridhar, S., Makrigiorgos, G. M., & Cormack, R. A. (2013). In vitro radiosensitization by gold nanoparticles during continuous low-dose-rate gamma irradiation with I-125 brachytherapy seeds. *Nanomedicine: nanotechnology, biology, and medicine*, *9*(1), 25–27. https://doi.org/10.1016/j.nano.2012.09.001

Orabi, M. (2026). Comparison of three LDR prostate brachytherapy treatment plans. *Nuclear Engineering and Technology*, *58*(1), 103901. https://doi.org/10.1016/j.net.2025.103901

Perl, J., Shin, J., Schumann, J., Faddegon, B., & Paganetti, H. (2012). TOPAS: an innovative proton Monte Carlo platform for research and clinical applications. *Medical physics*, *39*(11), 6818–6837. https://doi.org/10.1118/1.4758060

Poher, A., Berumen, F., Ma, Y., Perl, J., & Beaulieu, L. (2023). Validation of the TOPAS Monte Carlo toolkit for LDR brachytherapy simulations. *Physica Medica*, *107*, 102516. https://doi.org/10.1016/j.ejmp.2022.102516

Rezaei, H., Zabihzadeh, M., Ghorbani, M., Goli Ahmadabad, F., & Mostaghimi, H. (2017). Evaluation of dose enhancement in presence of gold nanoparticles in eye brachytherapy by ^{103}Pd source. *Australasian physical & engineering sciences in medicine*, *40*(3), 545–553. https://doi.org/10.1007/s13246-017-0555-1

Rivard, M. J., Coursey, B. M., DeWerd, L. A., Hanson, W. F., Saiful Huq, M., Ibbott, G. S., ... & Williamson, J. F. (2004). Update of AAPM Task Group No. 43 Report: A revised AAPM protocol for brachytherapy dose calculations. *Medical physics*, *31*(3), 633-674. https://doi.org/10.1118/1.1646040

Skowronek, J. (2017). Current status of brachytherapy in cancer treatment–short overview. *Journal of contemporary brachytherapy*, *9*(6), 581-589. https://doi.org/10.5114/jcb.2017.72607

Snyder, W. S., Cook, M., Nasset, E., Karhausen, L., & Tipton, I. (1975). Report of the task group on reference man. *Report prepared for international commission on radiological protection*, *23*, 46-57.

Taheri, A., Khandaker, M. U., Moradi, F., & Bradley, D. A. (2023). A review of recent advances in the modeling of nanoparticle radiosensitization with the Geant4-DNA toolkit. *Radiation Physics and Chemistry*, 111146. https://doi.org/10.1016/j.radphyschem.2023.111146